Journal of Materials Chemistry C

ROYAL SOCIETY OF CHEMISTRY

PAPER

View Article Online
View Journal | View Issue

Cite this: J. Mater. Chem. C, 2022, 10, 14496

Solution processable dithioalkylated methylidenyl cyclopentadithiophene based quinoidal small molecules for n-type organic field-effect transistors†

Shakil N. Afraj, ‡[a] Meng-Hao Lin,‡[b] Chih-Yao Wu,‡[c] Arulmozhi Velusamy,[a] Ping-Yu Huang,[a] Tzu-Yu Peng,[a] Jui-Chen Fu,[a] Shih-Hung Tung,[d] Ming-Chou Chen *[a] and Cheng-Liang Liu *[b]

A new series of cyclopentadithiophene (**CDT**)-based quinoidal semiconductors—**CDTSQ-8 (1)**, **CDTSQ-10 (2)**, **CDTSQ-12 (3)**, and **CDTSQ-14 (4)**—with various dithioalkylated-methylidenyl side chains were designed and synthesized as n-type organic small molecules for solution-processable organic field-effect transistors (OFETs). The physical, electrochemical, and electrical properties of these new compounds were thoroughly investigated. Further, single-crystal structures of **CDTSQ-10**, **CDTSQ-12**, and **CDTSQ-14** were obtained. Optimized geometries obtained from single-crystal X-ray diffraction revealed the planarity of the central core. The smaller dihedral angle between dithioalkyl methylene and the **CDT** core (4.8°), a planar molecular structure, short main-core stacking distance (3.43 Å), short intramolecular (S···H), and intermolecular (S···N, N···H, and N···N) distances of the **CDTSQ-12** molecule suggest good conditions for the extended π-orbital interaction of the corresponding molecule, resulting in better device performance. The favorable molecular packing and low-lying LUMO energy level (−4.10 eV) suggest that **CDTSQ**s could be electron-transporting semiconductors. Thin-film morphological analysis by grazing-incidence wide-angle X-ray scattering revealed that all **CDTSQ** molecules are stacked on the substrate in an edge-on fashion. OFETs based on solution-sheared **CDTSQ-12** exhibited the highest electron mobility of 0.14 $cm^2 V^{-1} s^{-1}$ with good ambient stability. The electron mobility of solution-processable **CDTSQ** is 14 times larger than that of a previously reported dilakylated-**CDT**-based **CDTRQ** (0.01 $cm^2 V^{-1} s^{-1}$, vacuum-processed) quinoidal derivative. These results demonstrate that side-chain engineering can improve the device performance of solution-sheared **CDTSQ** organic semiconductors.

Received 24th June 2022,
Accepted 15th August 2022

DOI: 10.1039/d2tc02679a

rsc.li/materials-c

Introduction

Design and synthesis of solution-processable π-conjugated organic semiconductors (OSCs) for various optoelectronic devices is one of the most active research fields and has attracted considerable attention for application in memory devices, smart cards, radio-frequency identification tags, transparent circuits, electronic papers, flexible displays, and sensors.[1–12] The design rule of these OSCs comprises a planar conjugated building block with suitable solubilizing alkyl side chains. The intermolecular/intramolecular interactions, molecular packing, and device performances can be significantly affected by the modifications of these alkyl side chains.[13–15] From a molecular design standpoint, the development of donor–acceptor (D–A)-type OSCs with a conjugated backbone has greatly advanced OFET technology,[16] resulting in several high-performance p-type (hole-transporting)[13,17–21] and n-type (electron-transporting) OSC families.[22–30] Despite considerable progress, the performance of n-type semiconductors continues to lag behind that of p-type semiconductors because of the critical requirements for lowest unoccupied molecular orbital (LUMO) energy levels and environmental trapping of electrons.[31–35] Hence, developing high-performance and ambiently stable n-type OSCs for OFETs is highly desirable.[28,36–40]

[a] Department of Chemistry and Research Center of New Generation Light Driven Photovoltaic Modules, National Central University, Taoyuan, 32001, Taiwan. E-mail: mcchen@ncu.edu.tw
[b] Department of Materials Science and Engineering, National Taiwan University, Taipei, 10617, Taiwan. E-mail: liucl@ntu.edu.tw
[c] Department of Chemical and Materials Engineering, National Central University, Taoyuan 32001, Taiwan
[d] Institute of Polymer Science and Engineering, National Taiwan University, Taipei 10617, Taiwan

† Electronic supplementary information (ESI) available. CCDC 2178823, 2178825 and 2178827. For ESI and crystallographic data in CIF or other electronic format see DOI: https://doi.org/10.1039/d2tc02679a

‡ These authors contributed equally to this work.

In addition, aromatic frameworks with conjugated cores functionalized with electron-withdrawing substituents are suitable building blocks for electron transport.[41–43] Among different OSC structural variations, dicyanomethylene (**DCN**)-substituted quinoidal oligothiophenes are excellent n-type semiconductors because of their high electron affinity originating from the quinoidal structure terminated by two strongly electron-withdrawing groups, affording low-lying LUMO energy levels.[44–46] The presence of a π-conjugated quinoidal core is known to strongly modulate the electronic structure.[22,47] The most prominent examples include electron-poor building blocks such as diketopyrrolopyrrole (**DPP**),[48] naphthalene diimide (**NDI**),[49–51] perylene carboxy diimide (**PDI**),[52] and other oligo/fused thiophene-based[53] cores optionally functionalized with electron-withdrawing functionalities such as perfluorophenyls,[54] cyanos,[55] and alkyl cyanoacetates.[56]

A fused-ring cyclopentadithiophene (**CDT**) derivative has attracted significant attention in the designing of small molecules and donor–acceptor polymers. This is due to its efficient electron-donating nature, facile synthesis from commercially available reagents, and simple side-chain manipulation for solubility.[57–59] For instance, Langa and coworkers reported a **CDT**-based A–D–A-type organic solar cell **FG4** (Fig. S1, ESI†) that exhibited a power conversion efficiency (PCE) of 8.43%.[60] Further, Bo and coworkers reported a **CDT**-based conjugated organic solar cell **NOC6F-1** (Fig. S1, ESI†) exhibiting a superior PCE of 10.62%.[61] Yang and coworkers reported an organic solar cell such as **2EH-CPDT(FBTTh$_2$)$_2$** (Fig. S1, ESI†) with the highest PCE of 3.2%.[62] On the polymer front, Bao and coworkers synthesized a **BDTup-CPDT** (Fig. S1, ESI†) polymer and demonstrated OFETs with a hole mobility of 0.044 $cm^2\ V^{-1}\ s^{-1}$.[63] Mullen and coworkers reported a **CDT-BTz** polymer[58] (Fig. S1, ESI†), which exhibited a field-effect mobility of 0.6 $cm^2\ V^{-1}\ s^{-1}$. Watson and coworkers reported a donor–acceptor copolymer semiconductor **P7** (Fig. S1, ESI†) based on an **NDI** acceptor with a **CDT** unit and used in n-channel OFETs, which exhibited an electron mobility of 0.006 $cm^2\ V^{-1}\ s^{-1}$.[50] Furthermore, Wu and coworkers reported a dye-sensitized solar cell **CPD1**[64] (Fig. S1, ESI†) comprising a **CDT** unit with *N*-annulated perylene exhibiting a PCE of 7.8%. In addition, Sun and coworkers reported hole-transporting materials **LYC-1** and **LYC-2**[65] (Fig. S1, ESI†) based on 4,4′-dimethoxy triphenylamine-substituted **CDT** and utilized in perovskite solar cells exhibiting a PCE of 19.07% and 17.60%, respectively.

Moreover, side chains significantly influence solution processability, intermolecular packing, and resulting film morphology. The solubilizing side chains attached to the conjugated backbone often disrupt the intermolecular ordering; thus, careful attention should be paid while designing them. The sp^2-hybridized side chains can be used to judiciously achieve material solubility with extended molecular planarity and crystalline packing interactions.[66] For example, a C=C double bond containing side chains was introduced at the 4-position of **CDT** to yield dithioalkylated-methylidenyl-**CDT**, permitting the alkyl chains to adopt a coplanar conformation and facilitate the small molecular backbone forming a close packing in the solid state to enhance charge carrier transportation.[67] Therefore, several research groups have developed dithioalkylated-methylidenyl-**CDT**-based small molecules and polymers. For instance, Woo and coworkers reported a dithioalkylated-methylidenyl-**CDT**-based semicrystalline p-type thermoelectric (TE) conjugated polymers **PCPDTSBT**[68] and **PCPDTSBT-A**[69] with the best power factor (PF) of 7.73 $\mu W\ m^{-1}\ K^{-2}$ and 40.4 $\mu W\ m^{-1}\ K^{-2}$ respectively (Fig. S2a, ESI†). Next, Woo and coworkers reported 4,9-dihydro-*s*-indaceno[1,2-*b*:5,6-*b*]-dithiophene (**IDT**)-based acceptor–donor–acceptor (A–D–A)-type OFETs such as **IDSIC-4F**[66] (Fig. S2b, ESI†) exhibits good hole and electron mobilities of 0.092 and 0.897 $cm^2\ V^{-1}\ s^{-1}$, respectively. Furthermore, similar **IDT**-based (A–D–A-type) OFETs such as **SEHIC**[67] (Fig. S2b, ESI†) reported by Noh and coworkers exhibited hole and electron mobilities of 0.148 and 0.023 $cm^2\ V^{-1}\ s^{-1}$, respectively (Fig. S2b, ESI†). In addition, Zhang and coworkers synthesized a donor–acceptor copolymer **PAFDTBT**[70] (Fig. S2c, ESI†) with a PCE of 6.2%. Furthermore, McCulloch and coworkers reported polymer **C10PAF**[71] (Fig. S2c, ESI†) with an enhanced field-effect mobility of 0.002 $cm^2\ V^{-1}\ s^{-1}$.

To date, different classes of conjugated materials exhibiting n-channel and ambipolar semiconducting properties[72,73] have been reported in the literature. In particular, fused planar aromatic structures are also known to enhance π–π stacking and hence induce high molecular ordering, which may lead to improved OFET performance with a simultaneous increase in charge transport properties.[74] Thus, several groups have addressed aromatic systems in a dicyanomethylene-substituted quinoidal structure affording organic n-channel semiconductors with electron mobilities.[15,26] For instance, Kunugi and coworkers reported a solution-deposited film of oligothiophene, **DCMT**,[75] (Fig. S3, ESI†) with a high electron mobility of 0.16 $cm^2\ V^{-1}\ s^{-1}$. Recently, our group has fabricated solution-processable n-type organic semiconductors such as **TSBTQ**[27] (Fig. S3, ESI†) and **DTTQ**,[44] (Fig. S3, ESI†) exhibiting electron mobilities of 0.45 and 0.18 $cm^2\ V^{-1}\ s^{-1}$, respectively. Moreover, Li and coworkers synthesized **CDT-2T(CN)$_4$**, (Fig. S3, ESI†) a n-type organic semiconductor that shows an electron mobility of 0.02 $cm^2\ V^{-1}\ s^{-1}$.[76] Similarly, Wurthner and coworkers reported a vacuum-processed **CDT**-based n-type organic semiconductor; **CPTQ-Oc**,[77] (Fig. S3, ESI†) (named **CDTRQ** in this paper) which showed an electron mobility of 0.01 $cm^2\ V^{-1}\ s^{-1}$. Marder and coworkers reported the synthesis, characterization, and charge transport properties of **DSP** (Fig. S3, ESI†) derivatives with an electron mobility of 0.00087 $cm^2\ V^{-1}\ s^{-1}$ in spin-cast layers.[78] Furthermore, Marks and coworkers were the pioneers of oligothiophenes end-capped with the fluoroalkyl/perfluorophenyl group as n-type semiconductors. They fabricated a **DFHCO-4T**-based (Fig. S4, ESI†) OFET device and optimized it to achieve an excellent electron mobility of up to 2.0 $cm^2\ V^{-1}\ s^{-1}$. Later, the same research group explored fused oligothiophenes end-capped with perfluorophenyl as n-type materials for OFETs and achieved an electron mobility up to 0.3–0.43 $cm^2\ V^{-1}\ s^{-1}$[53,79,80] (Fig. S4, ESI†).

In this study, we incorporated various dithioalkylated-methylidenyl side chains on the 4-position of the **CDT** unit. A dithioalkylated-methylidenyl-**CDT** unit has a sp^2-hybridized carbon atom at 4-position of **CDT** unit. Compared with

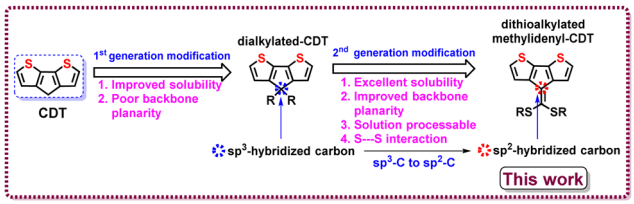

Fig. 1 Schematic illustration of incorporating dithioalkylated methylidenyl side chain at the 4-position of **CDT** unit to improve the backbone planarity.

dialkylated **CDT**,[77] the dithioalkylated methylidenyl-**CDT** backbone exhibits improved planarity and thus enhanced π–π stacking and S···S intermolecular interactions (see Fig. 1 for schematic illustration).

Inspired by these findings, we synthesized dithioalkylated methylidenyl-**CDT** central core-based quinoidal semiconductors, namely, **CDTSQ-8 (1)**, **CDTSQ-10 (2)**, **CDTSQ-12 (3)**, and **CDTSQ-14 (4)**. Dithioalkylated methylidenyl side chains containing **CDTSQ**s show excellent solubility in common organic solvents, which is beneficial for solution processability. To the best of our knowledge, dithioalkylated methylidenyl-**CDT**-based quinoidal semiconductors have never been reported. Furthermore, the physical, electrochemical, and electrical properties of **CDTSQ**s (**1–4**) were thoroughly investigated. Single-crystal structures of **CDTSQ-10 (2)**, **CDTSQ-12 (3)**, and **CDTSQ-14 (4)** were obtained to gain further insight into their molecular packing pattern and charge transport properties. Incidentally, crystal structures of dithioalkylated methylidenyl-**CDT** central backbone or corresponding organic semiconductors have never been reported. Next, semiconductor film deposition optimization was realized by semiconductor processing using solution-shearing methods *versus* conventional spin-coating. Thus, OFET performance and thin-film morphology were investigated as a function of processing methods demonstrating the superiority of shearing in enhancing molecular order and carrier mobility. In particular, among quinoidal series, **CDTSQ-12** exhibits the highest OFET electron mobility of 0.14 cm^{-2} V^{-1} s^{-1}, which is comparatively higher than that of dialkylated-**CDT**-unit-based organic semiconductors such as **CDT-2T(CN)$_4$** and **CPTQ-Oc**.[76,77] The electron mobility of solution-processable **CDTSQ** is 14 times larger than that of a previously reported dilakylated-**CDT**-based **CDTRQ** (0.01 cm^2 V^{-1} s^{-1}, vacuum-processed) quinoidal derivative.[77] These results demonstrate that side-chain engineering can improve the device performance of solution-sheared **CDTSQ** organic semiconductors.

Results and discussion

Synthesis

The synthetic route to quinoids **1–4** is shown in Scheme 1, where the starting molecule **CDT** (**5**) was synthesized following procedures from the literature.[81] First, compound **5** was deprotonated with *t*-BuOK and then treated with CS_2 for the *in situ* generation of the ketene dithiolate anion, which underwent alkylation with alkyl bromides ($C_8H_{17}Br$, $C_{10}H_{21}Br$, $C_{12}H_{25}Br$,

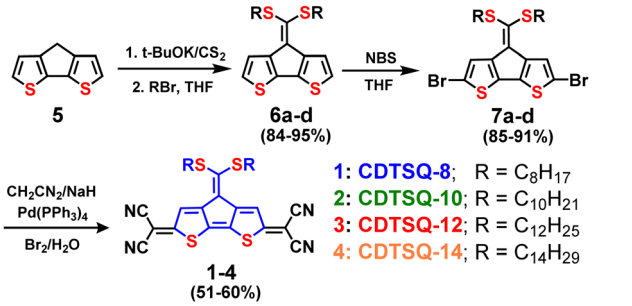

Scheme 1 Synthetic route to quinoidal semiconductors **CDTSQs** (**1–4**).

and $C_{14}H_{29}Br$) to afford the corresponding dialkylated thioacetals **6a–d** in excellent yields (84–95%). Upon further treatment of **6a–d** with *n*-bromosuccinimide, the dibrominated compounds **7a–d** were obtained in excellent yields (85–91%). Finally, *via* Takahashi coupling of compounds **7a–d** with malononitrile in the presence of $Pd(PPh_3)_4$ catalyst, followed by oxidation using a saturated solution of bromine in water, quinoids **CDTSQ 1–4** were obtained in good yields (51–60%) (Scheme 1). Further, dialkylated-**CDT**-based quinoidal derivative **CDTRQ** was synthesized using a procedure reported previously.[77]

Physical characterization

Thermal analyses of the new organic semiconductors **CDTSQ**s (**1–4**) were performed using differential scanning calorimetry (DSC; Fig. S5, ESI†) and thermogravimetric analysis (TGA; Fig. S6, ESI†); the corresponding thermal data are summarized in Table 1. The TGA measurements reveal that all four **CDTSQ**s (**1–4**) exhibit high thermal stability with ~5% weight loss starting in the temperature range of 305 °C–309 °C and at 317 °C for **CDTRQ** (Fig. S7, ESI†). The DSC scans reveal that all compounds **CDTSQ**s (**1–4**) have high melting points with sharp endotherms between 220 °C and 238 °C. Upon increasing the lengths of the side chain in **CDTSQ**s, the melting temperature decreases because chain motion at high temperatures reduces core–core intermolecular interactions. Thus, **CDTSQ-12 (3)** shows a sharp melting at 226 °C and a sharp crystallization peak at 205 °C, indicative of the highly ordered crystalline structures. Furthermore, a comparison of the effect of dialkylated and dithioalkylated-methylidenyl side chains in the **CDTRQ** and **CDTSQ** semiconductors, respectively, indicates that the melting temperature significantly decreases for **CDTRQ** (142 °C)[77] compared with that of **CDTSQ** (238 °C). This implies that **CDTSQ**s exhibiting better thermal behaviour due to the presence of dithioalkylated-methylidenyl side chains. The optical properties of **1–4** were measured using UV-Vis spectroscopy in diluted *o*-dichlorobenzene solution. As shown in Fig. 2, the solution absorption spectra of **CDTSQ**s (**1–4**) are identical to two main absorption bands, indicating that the variation of the thioalkyl side-chain length does not lead to fundamental changes in the intrinsic electronic structure of the π-conjugated **CDTS** backbone. By contrast, **CDTRQ** molecules, which do not have dithioalkylated-methylidenylide chains exhibiting a slight blue shift around

Table 1 Thermal, optical, and electrochemical Properties of **CDTSQ**s (**1–4**) and **CDTRQ**

Compound	T_d[a] [°C]	T_m[b] [°C]	λ_{max} (soln)[d] [nm]	λ_{max} (film)[e] [nm]	E_{ox}[f] [V]	HOMO[g] [eV]	E_{red}[f] [V]	LUMO[g] [eV]	ΔE_g (DPV)[h] [eV]
CDTSQ-8 (1)	307	238	552	513	1.88	−6.08	−0.12	−4.08	2.00
CDTSQ-10 (2)	309	231	552	514	1.90	−6.10	−0.10	−4.11	2.00
CDTSQ-12 (3)	307	226	552	513	1.90	−6.10	−0.10	−4.11	2.00
CDTSQ-14 (4)	305	220	552	509	1.89	−6.09	−0.13	−4.07	2.02
CDTRQ	317	142[c]	531	561[c]	1.98	−6.18	0.12	−4.08	2.10

[a] Decomposition temperature were determined from TGA. [b] Melting temperatures were determined from DSC. [c] Obtained from ref. 77. [d] Absorption spectra were measured in *o*-$C_6H_4Cl_2$. [e] Thin films were solution-sheared onto a quartz glass. [f] By DPV in *o*-$C_6H_4Cl_2$ at 25 °C. All potentials are reported with reference to an Fc/Fc^+ internal standard (at +0.6 V). [g] Using HOMO/LUMO = $-(4.2 + E_{ox}/E_{red})$. [h] The energy gap was calculated from the difference between HOMO and LUMO measured by DPV.

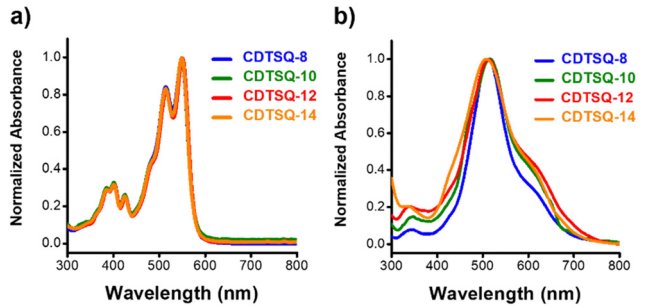

Fig. 2 (a) UV-vis absorption spectra of **CDTSQ**s (**1–4**) in diluted *o*-dichlorobenzene solution and (b) **1–4** thin film.

531 nm (Fig. S8, ESI†). In the **CDTSQ**s, the peak at 350–450 nm originated from the π–π^* transition through the conjugated backbone, while the peak at 450–580 nm for **CDTSQ**s was attributed to the intramolecular charge transfer (**ICT**) from the electron-donating **CDT** core and the electron-withdrawing cyano end groups.[66,68] The absorption edges of **CDTSQ**s in the film state are around 690 nm, corresponding to the estimated optical bandgaps of 1.82, 1.81, 1.77, and 1.81 eV for **CDTSQ-8**, **CDTSQ-10**, **CDTSQ-12**, and **CDTSQ-14**, respectively.

The absorption shoulder (~620 nm) can be found from the diluted solution to the thin films, indicating a strong π–π packing. It can be clearly seen that the most intensified absorption shoulder of **CDTSQ-12** is due to the better film formation from its increased solubility. By contrast, further increase in thioalkyl length for **CDTSQ-14** results in a decrease in the shoulder intensity, possibly due to an over-length side chain. The side-chain configuration is hypothesized to discernibly alter the aggregation state of **CDTSQ**s. Molecular energy levels of **CDTSQ**s (**1–4**) examined using differential pulse voltammetry (DPV) measurements are shown in Fig. 3 and Table 1. The DPV data show that all the **CDTSQ** quinoidal molecules possess similar oxidation and reduction potentials.

Thus, thioalkyl substituents of the conjugated backbones have no significant effect on the electrochemical properties of the **CDTSQ**s. In general, a nonthiolakylated **CDTRQ** molecule exhibits low highest occupied molecular orbital (HOMO) and high LUMO, which leads to the larger energy gap and thus inferiority to OFETs (Fig. S9, ESI† and Table 1). Consequently, the derived HOMO and LUMO of **1–4** and **CDTRQ** are located around −6.08, −6.10, −6.10, −6.09, and −6.18 eV and −4.08, −4.11, −4.11, −4.07, and −4.08 eV respectively, according to the equation HOMO/LUMO = $-(4.2 + E_{ox}/E_{red})$, assuming an internal standard ferrocene/ferrocenium (Fc/Fc^+) oxidation at −4.8 eV. The low-lying LUMO energy level of these **CDTSQ**s should lead to facile electron injection in OFETs and demonstrate the potential ambient stability of these n-type **CDTS** quinoids. To gain further insight into the effect of side-chain engineering on the electronic structure and molecular geometry of **CDTSQ**s (**1–4**), density functional theory (DFT) calculations were performed at the B3LYP/6-31G* level of the Gaussian 09W program. All the calculated compounds showed similar electron density distribution for HOMO and LUMO along the entire quinoidal backbone. This electron density distribution demonstrated a significant delocalization of the quinoidal structure. From the DFT calculations, all the HOMO and LUMO energy levels were calculated to be −6.29 and −3.95 eV, respectively, consistent with the DPV experimental results (Fig. 4). The optimized geometries obtained from DFT calculations (Fig. S10, ESI†) suggest that the **CDTSQ**-conjugated cores are highly planar, which would promote an efficient delocalization of the π-electrons and facilitate π–π overlap and intermolecular interactions; therefore, it could be beneficial for charge transport.

Single-crystal structure

Single crystals of **CDTSQ-10 (2)**, **CDTSQ-12 (3)**, and **CDTSQ-14 (4)** were grown *via* slow solvent evaporation using DCM/hexane solvent mixture to gain further insight into their molecular packing pattern and charge transport properties. Their molecular structure and the complete crystal data derived from X-ray crystallographic analyses are shown in Fig. 5 and Fig. S11, S12 (ESI†). Both **CDTSQ-10 (2)** and **CDTSQ-12 (3)** crystallize in the monoclinic space group of $P\bar{2}$ (Tables S1 and S2, ESI†), whereas **CDTSQ-14** recrystallizes in the triclinic space group of $P\bar{1}$ (Table S3, ESI†). Shorter distances between S(alkyl)···H(thiophene), 2.70 Å for **CDSTQ-10** (2), 2.70 and 2.71 Å for **CDSTQ-12** (3), and 2.76 and 2.73 Å for **CDSTQ-14**, showed the existence of an intramolecular nonbonded interaction between sulfur and hydrogen atoms. Those distances are lesser than the sum of the van der Waals radii of S and H atoms (3.0 Å). The dihedral angles between dithioalkyl methylene and the central core were 5.3°, 4.8°, and 4.9° for **CDSTQ-10**, **CDSTQ-12**, and **CDSTQ-14** molecules, respectively. The shorter dihedral angles were

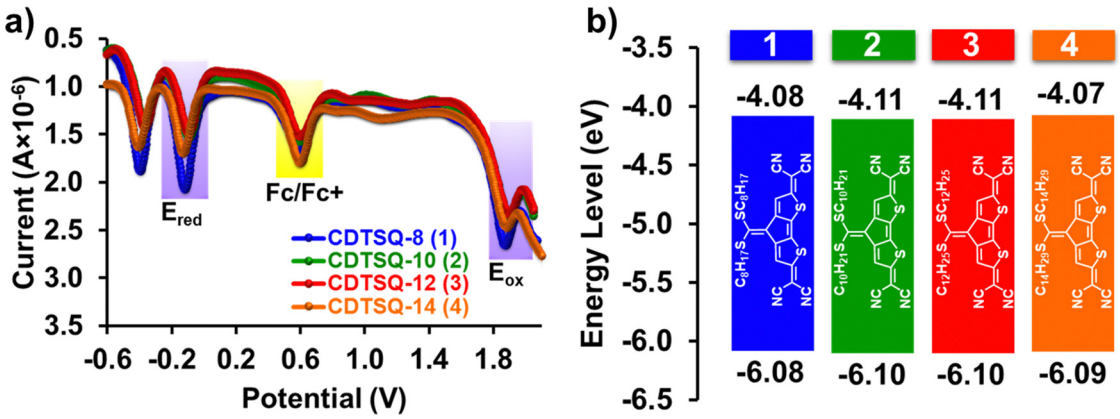

Fig. 3 (a) DPV response curves of **CDTSQ**s in *o*-dichlorobenzene. (b) DPV-derived HOMO and LUMO energy levels.

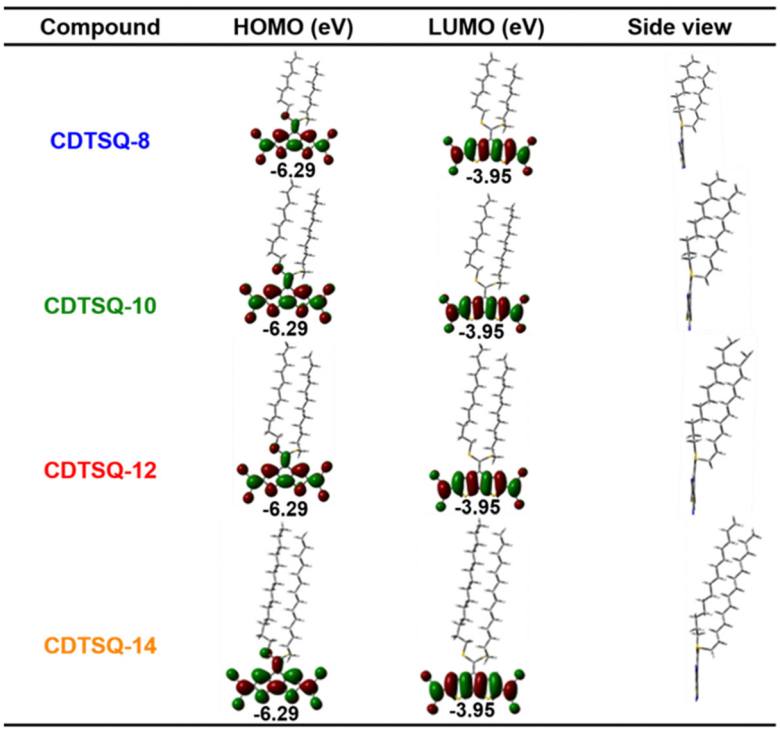

Fig. 4 DFT-derived HOMO and LUMO of **CDTSQ**s (**1–4**).

2.8 and 4.2° for molecule **2**, 2.6 and 4.3° for molecule **3**, and 2.3 and 4.4° for molecule **4** between the end-capping unit and central core (**CDT**), indicating good planarity of these **CDTSQ**s for efficient charge transfer (Fig. 5a and Fig. S11a, S12a, ESI†). The molecular lengths were 12.26, 12.32, and 12.33 Å for **CDSTQ-10**, **CDSTQ-12**, and **CDSTQ-14**, respectively. The front and side views of **CDTSQ** molecules with π–π interplanar distances of 3.43 Å exhibited brick-type π–π stacking arrangement (Fig. 5b, c and Fig. S11b, c, S12b, c, ESI†). Further, the shortest intermolecular S (fused core)···N distances of 2.98–3.02 Å, S (thioalkyl)···N distance of 3.26 Å, and N···H interaction of 2.69 Å–2.73 Å between **CDTSQ** layered molecules increase the order of π–π molecular stacking (Fig. 5d and Fig. S11d, S12d, ESI†). The molecular packing arrangement of **CDTSQ** molecules with a brick-type stacking distance of 3.43 Å exhibited an N···N intermolecular distance of 3.02–3.05 Å and slipping angles of 34.6°–39.5° and 94.5°–95.3° along the long and short molecular axes, respectively (Fig. 5e–g and Fig. S11e–g, S12e–g, ESI†). In summary, the smaller dihedral angles between dithioalkyl methylene and the **CDT** core (4.8°–5.3°), planar molecular structure, short main-core stacking distance (3.43 Å), and short intramolecular (S···H) and intermolecular (S···N, N···H, and N···N) distances of **CDSTQ** molecules suggest good conditions for the extended π-orbital interaction of the corresponding molecules, resulting in better OFET device performance.

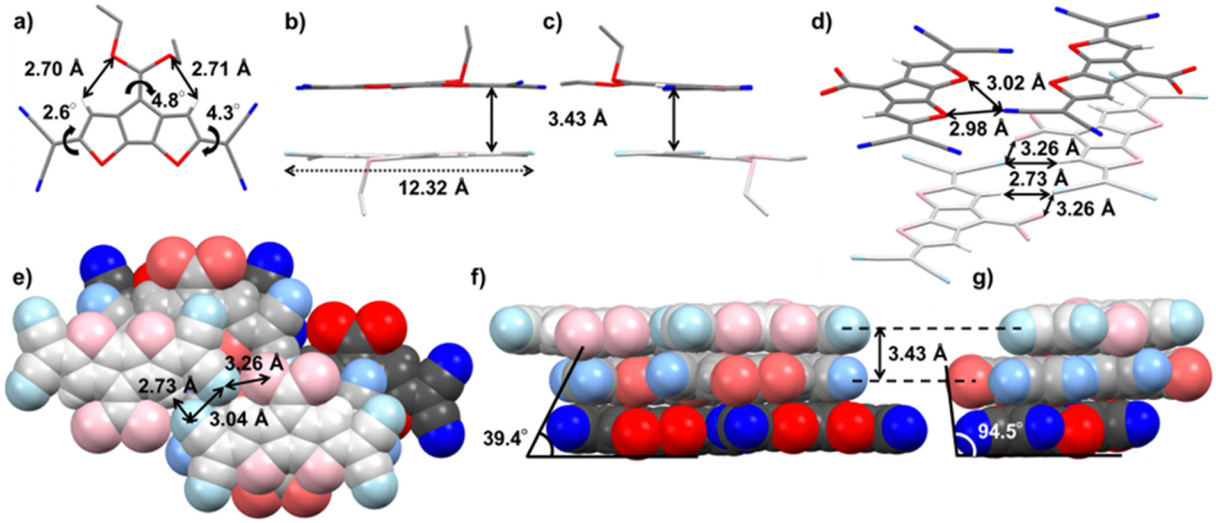

Fig. 5 Single crystal structure of **CDTSQ-12 (3)** in stick models (a–d) and space-filling models (e–g). Sulfur and nitrogen atoms are specified in red and blue colors. Alkyl chains are omitted for clarity. (a) Top view of **CDTSQ-12 (3)** with intramolecular S···H distance of ~2.71 Å and the shorter dihedral angles (2.6° and 4.3°) between the end-capping unit and central core. The dihedral angles between dithioalkyl methylene and CDT core is 4.8°. (b and c) Front-view and side-view of **CDTSQ** molecules with $\pi-\pi$ interplanar distances of 3.43 Å exhibiting brick type $\pi-\pi$ stacking arrangement. The molecular length is 12.32 Å for **CDSTQ-12** (**3**). (d) Shortest intermolecular S (fused core)···N distances of 2.98, 3.02 Å, S (thioalkyl)···N distance of 3.26 Å and N···H interaction of 2.73 Å between **CDTSQ** layered molecules increases the order of $\pi-\pi$ molecular stacking. (e–g) Molecular packing arrangement of **CDTSQ** molecules with a brick type stacking distance of 3.43 Å and exhibits the N···N intermolecular distance of 3.04 Å and slipping angles of 39.4° and 94.5° along the long and short molecular axes respectively.

Charge transport properties

To study the influence of different lengths of the alkylthio side chain on the electrical properties of **CDTSQ**s, the top contact/bottom gate (TC/BG) device architectures of OFETs were fabricated with the solution-sheared or spin-coated organic semiconductor layer to evaluate their charge transport characteristics and compare the performance of these two thin-film-processing techniques. The solution-shearing technique, which was successfully used in our previous work,[14] involves placing an organic semiconductor solution between the upper shearing plate and a bottom heated substrate, forming a confined meniscus and then displacing the plate at a constant speed. The details of device fabrication and measurement are described in the experimental section. Fig. 6a illustrates transfer curves of solution-sheared OFETs, in which the drain voltage (V_d) is fixed at 100 V. The cut-off characteristics are clearly observed for all four samples.

All **CDTSQ**-based devices exhibit a positive gate bias-modulated charge transport, indicating an apparent n-type semiconducting channel. This may be attributed to their relatively deep LUMOs. Fig. 6b and Fig. S14, S15, ESI† present the output characteristics of **CDTSQ**-based OFETs. The OFETs display clear current pinch-off and saturation behavior, implying that the gate voltage (V_g) can fully control the active channel drain current (I_d). Table 2 summarizes the mobility (μ), threshold voltage (V_{th}), and current ON/OFF current ratio (I_{ON}/I_{OFF}) of the four **CDTSQ**-based OFETs. The values of μ and V_{th} are extracted from the intercept at V_g and the slope of the plot of the square root of I_d *vs.* V_g, respectively. Different batches and cells in the same batch of characterized OFETs allow

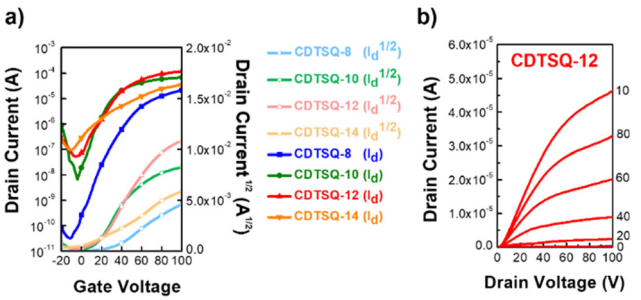

Fig. 6 Transfer characteristics of solution-sheared **CDTSQ**s OFETs.

Table 2 Summary of OFETs electrical parameters for solution-sheared **CDTSQ**s films

Compound	μ_{max} [cm^2 V^{-1} s^{-1}]	μ_{avg} [cm^2 V^{-1} s^{-1}]	I_{ON}/I_{OFF} [V]	V_{th} [V]
CDTSQ-8	0.025	0.016 ± 0.005	10^3–10^5	29.3 ± 6.7
CDTSQ-10	0.09	0.07 ± 0.01	10^3–10^4	8.9 ± 5.4
CDTSQ-12	0.14	0.09 ± 0.02	10^3–10^5	12.5 ± 2.4
CDTSQ-14	0.025	0.021 ± 0.004	10^2–10^3	17.8 ± 5.5

calculation of the statistical behavior of the device's electrical properties, using 10 data values for each. Among these four different alkylthio side-chain lengths of **CDTSQ** devices, **CDTSQ-12** exhibited the best performance, which displayed maximum and average electron mobilities of 0.14 cm^2 V^{-1} s^{-1} (μ_{max}) and 0.09 ± 0.02 cm^2 V^{-1} s^{-1} (μ_{avg}), respectively, with I_{ON}/I_{OFF} of 10^3–10^5. OFETs with solution-sheared **CDTSQ-8**, **CDTSQ-10**, and **CDTSQ-14** had a μ_{max}/μ_{avg} of 0.025/0.016 ± 0.005,

0.09/0.07 ± 0.01, and 0.025/0.021 ± 0.004 $cm^2 V^{-1} s^{-1}$, respectively. These results show that when the lengths of the alkylthio side chain increase, the electron mobility also improves under the condition that the number of carbon atoms in the side chain is not more than 12. Apparently, when the lengths of the alkylthio side chain increased to that of the tetradecylthio unit, the mobility of the devices suddenly dropped, which did not follow the abovementioned tendency. The comprehensive reason will be discussed in thin-film morphology and microstructural analysis. However, the threshold voltage (V_{th}) of solution-sheared OTFTs was very high (9–30 V), which may have resulted from a thicker film. Because of the TC/BG device architectures, the injected charges need to penetrate a very large depletion region before they reach the channel, which causes extra resistance between the source/drain electrodes and the semiconductor layer.

A comparison of solution-sheared OTFTs with spin-coated OTFTs revealed that the electron mobilities of solution-shearing-based devices were much higher than those of spin-coating-based devices, which can be seen in Fig. S13 and Table S4 (ESI†). This phenomenon could be attributed to two main reasons: first, the solution-shearing method provides a unidirectional shearing force that endows an organic semiconductor layer with highly aligned crystals, which favors charge carrier transport in the channel. Second, because of the low viscosity of the small-molecule solution, most of the solution would be spun off from the substrate, thus making the thin-film formability inferior, which causes more defects in devices and potentially reduces the crystallinity.

Morphological analysis

Fig. 7a–d display the polarized optical microscopy (POM) images of the four solution-sheared **CDTSQ** crystalline films. It can be visually observed that all the samples possess an aligned long-plate-like crystal texture covering the substrate surface and parallel with the shearing direction, which is the typical feature of the solution-sheared films with optimization between the shearing rate and solvent evaporation.[80] However, the POM image of **CDTSQ-8** shows many cross-shaped precipitates inside the crystals, which is probably due to the early nucleation during the shearing process that leads to the irregular and disordered crystal structure, resulting from the lower solubility of the shortest alkylthio side-chain lengths in **CDTSQ-8**. When the alkylthio side-chain lengths increase, this effect could be alleviated, as observed in the cases of **CDTSQ-12** and **CDTSQ-14**, which may give rise to a high degree of crystallinity and crystallographic alignment of the large-sized crystals. Fig. S16a–d (ESI†) show the spin-coated **CDTSQ** films to compare the difference between these two processing techniques. The crystals of the spin-coated **CDTSQ** films are tattered on the entire film, and there are no continuous crystal domains to facilitate charge transport. Further, tapping-mode atomic force microscopy (AFM) was also used to study the morphologies of the crystalline films. Fig. 7e–h exhibit the topographic images of the solution-sheared **CDTSQ** thin films, and their root-mean-square roughness (R_{rms}) are reported. The crystals of all the **CDTSQ** samples are plate-like and parallel with the direction of the solution shearing, but the R_{rms} varies. An increased R_{rms} is known to be related to a larger crystal domain. The R_{rms} values were 2.3, 4.3, 6.6, and 4.8 nm for the samples of **CDTSQ-8**, **CDTSQ-10**, **CDTSQ-12**, and **CDTSQ-14**, respectively. The larger R_{rms} and fewer grain boundaries of **CDTSQ-12** imply a larger crystal domain that can lead to better charge transport. This result coincides with the semiconducting electrical property. The AFM images of the spin-coated **CDTSQ** films can be seen in Fig. S16e–h, (ESI†) which shows that the spin-coated films contain tiny disordered crystals. Consequently, the spin-coated devices exhibited very poorer electrical behavior.

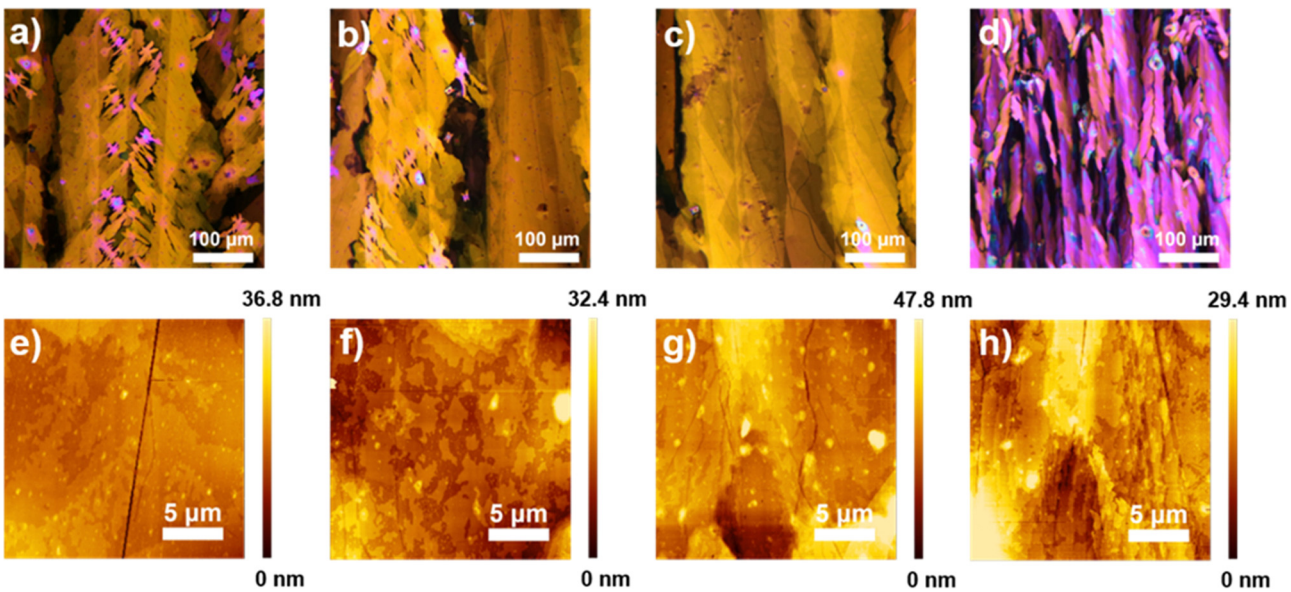

Fig. 7 POM (upper) and AFM (lower) images of solution-sheared (a and e) **CDTSQ-8**, (b and f) **CDTSQ-10**, (c and g) **CDTSQ-12**, and (d and h) **CDTSQ-14**.

Microstructural analysis

GIWAXS analysis was conducted to understand the effect of different alkylthio side-chain lengths on the molecular packing and crystallinity of **CDTSQ**s. The diffractogram and corresponding packing parameters of solution-sheared **CDTSQ-8**, **CDTSQ-10**, **CDTSQ-12**, and **CDTSQ-14** can be found in Fig. 8 and Table S5 (ESI†). The GIWAXS patterns show intense Bragg spots for these solution-sheared films. All **CDTSQ**s demonstrate the apparent (00*l*) lamellar spotty reflection in the out-of-plane direction (q_z), indicating a typical edge-on molecular orientation, which may facilitate charge transport in the OFET channel. The order of diffraction appearing in the patterns is found to be affected by the side-chain length. As the alkylthio side-chain length increases, the higher-order diffraction spots can be seen until 12 carbons. **CDTSQ-12** reaches the highest diffraction order (l = 3), probably resulting from the longer side chain that causes the higher solubility and thus prevents the disordered nucleation sites during the shearing process. However, the **CDTSQ-14** sample does not follow this trend. A possible reason could be that the overlength side chain disturbs the lamellar molecule packing. The lamellar spacing calculated from the primary peaks of **CDTSQ**s is listed in Table S5 (ESI†). As expected, the lamellar spacing increases with side-chain length, from 24.15 to 33.74 Å as the side-chain length increases from 8 to 14 carbons. In addition, judging from the intensity of the (10*l*) signals, considered as the π–π intermolecular interaction, the intensity of the (10*l*) signals follows a similar trend with the diffraction order of (00*l*) peak. When the side-chain length increases from 8 to 12 carbons, the (10*l*) signals become more distinct. **CDTSQ-12** has the shortest π–π stacking distance of 3.43 Å, which benefits charge transport in OFETs. However, for **CDTSQ-14**, the intensity of the (10*l*) signal sharply weakens and the π–π stacking distance increases compared with **CDTSQ-12**. Again, this indicates that the 12-carbon side chain is optimal for the **CDTSQ** small-molecule semiconductors.

Further, using the GIWAXS patterns and single-crystal data, the molecular packing in the thin-film state was proposed. A comparison of the length of the *c*-axis from single-crystal data and lamellar distance from GIWAXS indicates that the **CDTSQ** molecules may align with the *c*-axis, as shown in Fig. S17 (ESI†). Furthermore, the crystal long axis (*b*-axis) aligns parallel to the shearing direction where the crystallographic *ac*-plane is perpendicular to the substrate surface. To acquire more detailed structure information, the 1D profiles of the (00*l*) lamellar diffractions in the out-of-plane direction are compared in Fig. S18 (ESI†). The full width at half maximum (FWHM) and the crystal coherence length (L_c) of the four samples, summarized in Table S5, (ESI†) demonstrate the same tendency of grain size as that from the AFM images. **CDTSQ-12** has the sharpest and narrowest diffraction peak among the four samples, suggesting the highest crystallinity and largest crystal grain size. Semiconducting channels with larger crystals can alleviate the charge transport hindrance from the grain boundaries. Thus, **CDTSQ-12** shows the highest charge mobility in the OFET measurements. The diffraction patterns of the spin-coated films are shown in Fig. S19 (ESI†). In contrast to the patterns of the solution-sheared films, all the spin-coated **CDTSQ**s exhibit lower diffraction orders and weaker diffraction from π–π intermolecular interaction. This result may be due to the nondirectional film-forming process, the inferior

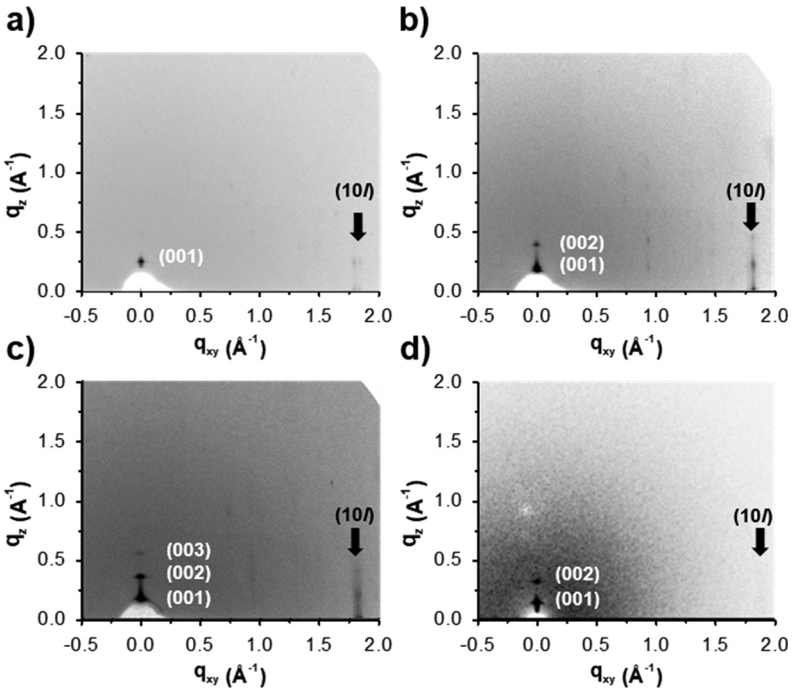

Fig. 8 2D GIWAXS patterns of solution-sheared (a) **CDTSQ-8**, (b) **CDTSQ-10**, (c) **CDTSQ-12**, and (d) **CDTSQ-14** films.

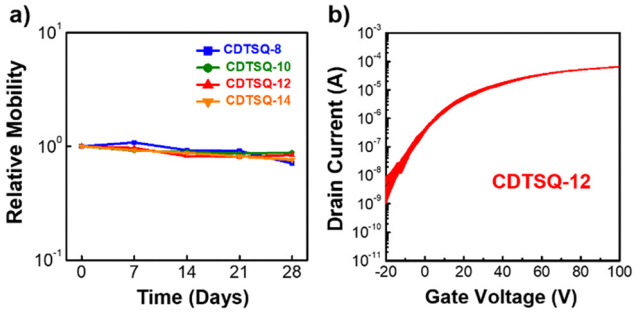

Fig. 9 (a) Long-term ambient stability of **CDTSQ**s OFETs. (b) Multiple gate sweeps of **CDTSQ-12** OFETs for 100 cycles.

thin-film formability, and the relatively disordered nucleation sites during spin coating, resulting in lower crystallinity.

Device stability test

The long-term environmental stability of four **CDTSQ** samples was estimated by measuring the device mobility every seven days when it was stored in the ambient environment (relative humidity 45–50% and room temperature of 25 °C). As shown in Fig. 9a, the mobility of all **CDTSQ** OFETs does not decline for 28 days, which can be ascribed to the introduction of the strong electron-withdrawing cyano end-capping groups. After attaching four cyano groups to the quinoidal **CDTS** core, their LUMO energy levels decreased to −3.95 eV, which may increase the tolerance of H_2O/O_2. Moreover, to evaluate the device's operational stability, electrical sweeps with V_g ranging from −20 to 100 V with a fixed V_d = 100 V were repeated for 100 cycles. As seen in Fig. 9b and Fig. S20, (ESI†) the transfer characteristics of the four OFETs do not change markedly. This good reliability can be due to the surface passivation between the organic semiconductor and dielectric layers. The surface trap problems can be alleviated through self-assembled monolayer (SAM) passivation. Consequently, the devices can retain their electrical performance after 100 operation cycles.

Conclusion

In conclusion, new series of dithioalkylated-methylidenyl **CDT**-based quinoidal semiconductors—**CDTSQ**s (**1–4**)—were designed and synthesized as solution-processable n-type organic small molecules for OFETs. Furthermore, single-crystal structures of **CDTSQ-10**, **CDTSQ-12**, and **CDTSQ-14** were obtained. The physical, electrochemical, as well as electrical properties of these new compounds were thoroughly investigated. **CDTSQ** with long side chains was found to improve solubility for efficient thin-film processing using the solution-shearing method, molecular packing, and charge transport characteristics, which favorably impact electron transport. The abovementioned observations are validated by analyzing optical absorption, microscopic images, and GIWAXS measurements. Among the **CDTSQ** derivatives, solution-sheared **CDTSQ-12** possesses the highest mobility of 0.14 $cm^2\ V^{-1}\ s^{-1}$ as well as good ambient and electrical stability, thus making it a promising new solution-processable and air-stable organic semiconductor for OFET applications.

Experimental

General synthetic procedures for final compounds (1–4)

Malononitrile (0.63 mmol) was added to a solution of sodium hydride (1.5 mmol) in dry THF (20 mL) at 0 °C, after the addition, reaction mixture was warmed to room temperature and stirred for 20 min. Next, compound (**7a–d**) (0.16 mmol) and tetrakis(triphenyl–phosphine)palladium (0.09 mmol) were added to the reaction mixture. The mixture was refluxed for 12 h, and then it was quenched with saturated bromine water at 0 °C and stirred for 15 min. The mixture was extracted with CH_2Cl_2, washed with brine, dried over Na_2SO_4, and evaporated. The residue was purified by column chromatography using CH_2Cl_2/hexanes (1 : 1).

Synthesis of CDTSQ-8 (1)

The title compound was obtained as a dark blue solid 0.049 g (yield = 51%). Mp: 242 °C. ^{1}H NMR (300 MHz, $CDCl_3$): δ 7.79 (s, 2H), 3.10 (t, J = 7.4 Hz, 4H), 1.75–1.65 (m, 4H), 1.40 (m, 4H), 1.30 (m, 16H), 0.87 (t, J = 10.5 Hz, 6H). ^{13}C NMR (125 MHz, $CDCl_3$): δ 176.58, 161.89, 158.81, 142.13, 124.67, 121.64, 112.95, 112.44, 72.78, 37.08, 31.72, 30.39, 29.06, 28.99, 28.79, 22.60, 14.05. HRMS (HR-FAB $[M]^+$) calcd for $C_{32}H_{36}N_4S_4$: 604.1823. Found: 604.1817.

Synthesis of CDTSQ-10 (2)

The title compound was obtained as a dark blue solid, 0.055 g (yield = 57%). Mp: 236 °C. ^{1}H NMR (500 MHz, $CDCl_3$): δ 7.79 (s, 2H), 3.11 (t, J = 7.5 Hz, 4H), 1.73–1.67 (m, 4H), 1.40 (m, 4H), 1.30 (m, 24H), 0.88 (t, J = 7.0 Hz, 6H). ^{13}C NMR (125 MHz, $CDCl_3$): δ 176.53, 161.87, 158.77, 142.08, 124.69, 121.65, 112.90, 112.43, 72.85, 37.07, 31.86, 30.39, 29.48, 29.40, 29.26, 29.02, 28.77, 22.65, 14.07. HRMS (HR-FAB $[M]^+$) calcd for $C_{36}H_{44}N_4S_4$: 660.2449. Found: 660.2443.

Synthesis of CDTSQ-12 (3)

The title compound was obtained as a dark blue solid, 0.060 g (yield = 60%). Mp: 231 °C. ^{1}H NMR (300 MHz, $CDCl_3$): δ 7.78 (s, 2H), 3.10 (t, J = 7.5 Hz, 4H), 1.74–1.64 (m, 4H), 1.40 (m, 4H), 1.30 (m, 32H), 0.87 (t, J = 11 Hz, 6H). ^{13}C NMR (125 MHz, $CDCl_3$): δ 176.54, 161.87, 158.78, 142.10, 124.68, 121.64, 112.91, 112.43, 72.83, 37.07, 31.90, 30.87, 30.38, 29.61, 29.53, 29.40, 29.33, 29.02, 28.78, 22.67, 14.08. HRMS (HR-FAB $[M]^+$) calcd for $C_{40}H_{52}N_4S_4$: 716.3075, Found: 716.3069.

Synthesis of CDTSQ-14 (4)

The title compound was obtained as a dark blue solid, 0.050 g (yield = 52%). Mp: 222 °C. ^{1}H NMR (300 MHz, $CDCl_3$): δ 7.78 (s, 2H), 3.10 (t, J = 7.5 Hz, 4H), 1.73–1.67 (m, 4H), 1.40 (m, 4H), 1.30 (m, 40H), 0.85 (t, J = 10 Hz, 6H). ^{13}C NMR (125 MHz, $CDCl_3$): δ 176.58, 161.90, 158.78, 142.10, 124.69, 121.65, 112.94, 112.46, 37.05,.31.93, 30.41, 29.69, 29.55, 29.42, 29.37, 29.04,

28.79, 22.70, 14.12. HRMS (HR-FAB $[M]^+$) calcd for $C_{44}H_{60}N_4S_4$: 772.3701, Found: 772.3695.

Device fabrication and measurement

This study used a heavily n-doped silicon wafer with 300 nm thermally grown SiO_2 dielectric as the substrate for OFETs. The substrates were sonicated with acetone and isopropanol each for 5 minutes. Subsequently, the substrates were dried with nitrogen and exposed under UV ozone plasma for 5 minutes. The dielectric surface was treated with (2-phenylethyl)trichlorosilane (PETS) to form the SAM for further passivation. The organic semiconductor layer was deposited onto the PETS-treated dielectric layer using the solution shearing method with 3 mg mL^{-1} **CDTSQ**s dissolved in chlorobenzene or 1,2,4-trichlorobenzene. The shearing speed ranged from 20 to 80 μm s^{-1}, and deposition temperature ranged from 90 °C to 110 °C under shearing. After deposition, the samples were thermally annealed at 100 °C for 1 hour under vacuum. Finally, silver source/drain electrodes that matched LUMO energy levels of **CDTSQ**s samples were deposited with shadow masks at a rate of 0.5 Å s^{-1}. A thermal evaporator controlled the chamber pressure at 10^{-6} torr. The channel will be perpendicular to the shearing direction and the channel length (L) and width (W) are 25 and 1500 μm, respectively. The OFETs electrical performance was measured inside the nitrogen-filled glove box by Keithley 4200-SCS with a probe station at room temperature and in the dark. The mobility (μ) was obtained from the following equation:

$$\mu = \frac{2L}{WC}\left(\frac{\partial\sqrt{I_d}}{\partial V_g}\right)^2 \quad (1)$$

where C is the capacitance per unit area of the dielectric layer.

Conflicts of interest

There are no conflicts to declare.

Acknowledgements

M.-C. C. thanks the financial support from the Ministry of Science and Technology (MOST) in Taiwan (109-2113-M-008-011-MY2) and NCU-Covestro Research Center (110-2622-8-008-007). C.-L. L. gratefully acknowledges the funding from the Young Scholar Fellowship Program (Columbus Program) and 2030 Cross-Generation Young Scholars Program by MOST in Taiwan, under Grant 110-2636-E-002-021 and 111-2628-E-002-014, respectively. The authors thank beamline TLS B13A1/B17A1 from the National Synchrotron Radiation Research Center (NSRRC) of Taiwan for providing beamtime.

Notes and references

1 E. K. Lee, M. Y. Lee, C. H. Park, H. R. Lee and J. H. Oh, *Adv. Mater.*, 2017, **29**, 1703638.
2 D. A. Taylor, J. A. Teku, S. Cho, W.-S. Chae, S.-J. Jeong and J.-S. Lee, *Chem. Mater.*, 2021, **33**, 4399–4407.
3 S. Fratini, M. Nikolka, A. Salleo, G. Schweicher and H. Sirringhaus, *Nat. Mater.*, 2020, **19**, 491–502.
4 Y. Pan and G. Yu, *Chem. Mater.*, 2021, **33**, 2229–2257.
5 Z.-F. Yao, J.-Y. Wang and J. Pei, *Chem. Sci.*, 2021, **12**, 1193–1205.
6 T. Okamoto, C. P. Yu, C. Mitsui, M. Yamagishi, H. Ishii and J. Takeya, *J. Am. Chem. Soc.*, 2020, **142**, 9083–9096.
7 L. Janasz, M. Borkowski, P. W. M. Blom, T. Marszalek and W. Pisula, *Adv. Funct. Mater.*, 2022, **32**, 2105456.
8 S. Yuvaraja, A. Nawaz, Q. Liu, D. Dubal, S. G. Surya, K. N. Salama and P. Sonar, *Chem. Soc. Rev.*, 2020, **49**, 3423–3460.
9 J. Wang, D. Ye, Q. Meng, C.-A. Di and D. Zhu, *Adv. Mater. Technol.*, 2020, **5**, 2000218.
10 C. Lubrano, G. M. Matrone, G. Iaconis and F. Santoro, *ACS Nano*, 2020, **14**, 12271–12280.
11 S. N. Afraj, D. Zheng, A. Velusamy, W. Ke, S. Cuthriell, X. Zhang, Y. Chen, C. Lin, J.-S. Ni, M. R. Wasielewski, W. Huang, J. Yu, C.-H. Pan, R. D. Schaller, M.-C. Chen, M. G. Kanatzidis, A. Facchetti and T. J. Marks, *ACS Energy Lett.*, 2022, **7**, 2118–2127.
12 S. N. Afraj, A. Velusamy, C.-Y. Chen, J.-S. Ni, Y. Ezhumalai, C.-H. Pan, K.-Y. Chen, S.-L. Yau, C.-L. Liu, C.-H. Chiang, C.-G. Wu and M.-C. Chen, *J. Mater. Chem. A*, 2022, **10**, 11254–11267.
13 S. N. Afraj, C.-C. Lin, A. Velusamy, C.-H. Cho, H.-Y. Liu, J. Chen, G.-H. Lee, J.-C. Fu, J.-S. Ni, S.-H. Tung, S. Yau, C.-L. Liu, M.-C. Chen and A. Facchetti, *Adv. Funct. Mater.*, 2022, **32**, 2200880.
14 S. Vegiraju, X.-L. Luo, L.-H. Li, S. N. Afraj, C. Lee, D. Zheng, H.-C. Hsieh, C.-C. Lin, S.-H. Hong, H.-C. Tsai, G.-H. Lee, S.-H. Tung, C.-L. Liu, M.-C. Chen and A. Facchetti, *Chem. Mater.*, 2020, **32**, 1422–1429.
15 S. Vegiraju, A. A. Amelenan Torimtubun, P.-S. Lin, H.-C. Tsai, W.-C. Lien, C.-S. Chen, G.-Y. He, C.-Y. Lin, D. Zheng, Y.-F. Huang, Y.-C. Wu, S.-L. Yau, G.-H. Lee, S.-H. Tung, C.-L. Wang, C.-L. Liu, M.-C. Chen and A. Facchetti, *ACS Appl. Mater. Interfaces*, 2020, **12**, 25081–25091.
16 M. Kim, S. U. Ryu, S. A. Park, K. Choi, T. Kim, D. Chung and T. Park, *Adv. Funct. Mater.*, 2020, **30**, 1904545.
17 C.-C. Lin, S. N. Afraj, A. Velusamy, P.-C. Yu, C.-H. Cho, J. Chen, Y.-H. Li, G.-H. Lee, S.-H. Tung, C.-L. Liu, M.-C. Chen and A. Facchetti, *ACS Nano*, 2021, **15**, 727–738.
18 S. N. Afraj, G.-Y. He, C.-Y. Lin, A. Velusamy, C.-Y. Huang, P.-S. Lin, S. Vegiraju, P.-Y. Huang, J.-S. Ni, S.-L. Yau, S.-H. Tung, T. Minari, C.-L. Liu and M.-C. Chen, *Adv. Mater. Technol.*, 2021, **6**, 2001028.
19 A. Velusamy, Y.-C. Yang, C.-C. Lin, S. N. Afraj, K. Jiang, P.-S. Chen, S.-L. Yau, I. Osaka, S.-H. Tung, M.-C. Chen and C.-L. Liu, *Adv. Electron. Mater.*, 2021, **8**, 2100648.
20 M.-C. Chen, Y.-J. Chiang, C. Kim, Y.-J. Guo, S.-Y. Chen, Y.-J. Liang, Y.-W. Huang, T.-S. Hu, G.-H. Lee, A. Facchetti and T. J. Marks, *Chem. Commun.*, 2009, 1846–1848.
21 S. Vegiraju, B.-C. Chang, P. Priyanka, D.-Y. Huang, K.-Y. Wu, L.-H. Li, W.-C. Chang, Y.-Y. Lai, S.-H. Hong, B.-C. Yu, C.-L. Wang, W.-J. Chang, C.-L. Liu, M.-C. Chen and A. Facchetti, *Adv. Mater.*, 2017, **29**, 1702414.

22 Y. Sun, Y. Guo and Y. Liu, *Mater. Sci. Eng. R: Rep.*, 2019, **136**, 13–26.
23 Y. Wang, L. Sun, C. Wang, F. Yang, X. Ren, X. Zhang, H. Dong and W. Hu, *Chem. Soc. Rev.*, 2019, **48**, 1492–1530.
24 A. F. Paterson, S. Singh, K. J. Fallon, T. Hodsden, Y. Han, B. C. Schroeder, H. Bronstein, M. Heeney, I. McCulloch and T. D. Anthopoulos, *Adv. Mater.*, 2018, **30**, 1801079.
25 S. Vegiraju, C.-Y. Lin, P. Priyanka, D.-Y. Huang, X.-L. Luo, H.-C. Tsai, S.-H. Hong, C.-J. Yeh, W.-C. Lien, C.-L. Wang, S.-H. Tung, C.-L. Liu, M.-C. Chen and A. Facchetti, *Adv. Funct. Mater.*, 2018, **28**, 1801025.
26 A. Velusamy, C.-H. Yu, S. N. Afraj, C.-C. Lin, W.-Y. Lo, C.-J. Yeh, Y.-W. Wu, H.-C. Hsieh, J. Chen, G.-H. Lee, S.-H. Tung, C.-L. Liu, M.-C. Chen and A. Facchetti, *Adv. Sci.*, 2021, **8**, 2002930.
27 V. Joseph, C.-H. Yu, C.-C. Lin, W.-C. Lien, H.-C. Tsai, C.-S. Chen, A. A. A. Torimtubun, A. Velusamy, P.-Y. Huang, G.-H. Lee, S.-L. Yau, S.-H. Tung, T. Minari, C.-L. Liu and M.-C. Chen, *J. Mater. Chem. C*, 2020, **8**, 15450–15458.
28 C. Zhang and X. Zhu, *Adv. Funct. Mater.*, 2020, **30**, 2000765.
29 S.-S. Cheng, P.-Y. Huang, M. Ramesh, H.-C. Chang, L.-M. Chen, C.-M. Yeh, C.-L. Fung, M.-C. Wu, C.-C. Liu, C. Kim, H.-C. Lin, M.-C. Chen and C.-W. Chu, *Adv. Funct. Mater.*, 2014, **24**, 2057–2063.
30 A. Velusamy, S. N. Afraj, S. Yau, C.-L. Liu, Y. Ezhumalai, P. Kumaresan and M.-C. Chen, *J. Chin. Chem. Soc.*, 2022, **69**, 1253–1275.
31 C. Wang, H. Dong, W. Hu, Y. Liu and D. Zhu, *Chem. Rev.*, 2012, **112**, 2208–2267.
32 J. Mei, Y. Diao, A. L. Appleton, L. Fang and Z. Bao, *J. Am. Chem. Soc.*, 2013, **135**, 6724–6746.
33 H. Li, F. S. Kim, G. Ren and S. A. Jenekhe, *J. Am. Chem. Soc.*, 2013, **135**, 14920–14923.
34 H. Li, T. Earmme, G. Ren, A. Saeki, S. Yoshikawa, N. M. Murari, S. Subramaniyan, M. J. Crane, S. Seki and S. A. Jenekhe, *J. Am. Chem. Soc.*, 2014, **136**, 14589–14597.
35 B. J. Jung, N. J. Tremblay, M.-L. Yeh and H. E. Katz, *Chem. Mater.*, 2011, **23**, 568–582.
36 Y. Ren, X. Yang, L. Zhou, J.-Y. Mao, S.-T. Han and Y. Zhou, *Adv. Funct. Mater.*, 2019, **29**, 1902105.
37 H. Jiang, S. Zhu, Z. Cui, Z. Li, Y. Liang, J. Zhu, P. Hu, H.-L. Zhang and W. Hu, *Chem. Soc. Rev.*, 2022, **51**, 3071–3122.
38 Z. S. Parr, J. Borges-González, R. B. Rashid, K. J. Thorley, D. Meli, B. D. Paulsen, J. Strzalka, J. Rivnay and C. B. Nielsen, *Adv. Mater.*, 2022, **34**, 2107829.
39 D. Qu, T. Qi and H. Huang, *J. Energy Chem.*, 2021, **59**, 364–387.
40 H. Sun, X. Guo and A. Facchetti, *Chem*, 2020, **6**, 1310–1326.
41 K. Kikuchi, J. Nakamura, Y. Nagata, H. Tsuchida, T. Kakuta, T. Ogoshi and Y. Morisaki, *Chem. – Asian J.*, 2019, **14**, 1681–1685.
42 Y. Teshima, M. Saito, T. Fukuhara, T. Mikie, K. Komeyama, H. Yoshida, H. Ohkita and I. Osaka, *ACS Appl. Mater. Interfaces*, 2019, **11**, 23410–23416.
43 S. Kumagai, H. Ishii, G. Watanabe, C. P. Yu, S. Watanabe, J. Takeya and T. Okamoto, *Acc. Chem. Res.*, 2022, **55**, 660–672.
44 S. Vegiraju, G.-Y. He, C. Kim, P. Priyanka, Y.-J. Chiu, C.-W. Liu, C.-Y. Huang, J.-S. Ni, Y.-W. Wu, Z. Chen, G.-H. Lee, S.-H. Tung, C.-L. Liu, M.-C. Chen and A. Facchetti, *Adv. Funct. Mater.*, 2017, **27**, 1606761.
45 C. Zhang, Y. Zang, E. Gann, C. R. McNeill, X. Zhu, C.-A. Di and D. Zhu, *J. Am. Chem. Soc.*, 2014, **136**, 16176–16184.
46 K. Feng, H. Guo, H. Sun and X. Guo, *Acc. Chem. Res.*, 2021, **54**, 3804–3817.
47 C. Zhang and X. Zhu, *Acc. Chem. Res.*, 2017, **50**, 1342–1350.
48 Y. Qiao, Y. Guo, C. Yu, F. Zhang, W. Xu, Y. Liu and D. Zhu, *J. Am. Chem. Soc.*, 2012, **134**, 4084–4087.
49 F. Würthner and M. Stolte, *Chem. Commun.*, 2011, **47**, 5109–5115.
50 X. Guo, F. S. Kim, M. J. Seger, S. A. Jenekhe and M. D. Watson, *Chem. Mater.*, 2012, **24**, 1434–1442.
51 S. Wang, H. Sun, T. Erdmann, G. Wang, D. Fazzi, U. Lappan, Y. Puttisong, Z. Chen, M. Berggren, X. Crispin, A. Kiriy, B. Voit, T. J. Marks, S. Fabiano and A. Facchetti, *Adv. Mater.*, 2018, **30**, 1801898.
52 H. Z. Chen, M. M. Ling, X. Mo, M. M. Shi, M. Wang and Z. Bao, *Chem. Mater.*, 2007, **19**, 816–824.
53 J. Youn, P.-Y. Huang, Y.-W. Huang, M.-C. Chen, Y.-J. Lin, H. Huang, R. P. Ortiz, C. Stern, M.-C. Chung, C.-Y. Feng, L.-H. Chen, A. Facchetti and T. J. Marks, *Adv. Funct. Mater.*, 2012, **22**, 48–60.
54 M.-H. Yoon, A. Facchetti, C. E. Stern and T. J. Marks, *J. Am. Chem. Soc.*, 2006, **128**, 5792–5801.
55 D. Huang, H. Yao, Y. Cui, Y. Zou, F. Zhang, C. Wang, H. Shen, W. Jin, J. Zhu, Y. Diao, W. Xu, C.-A. Di and D. Zhu, *J. Am. Chem. Soc.*, 2017, **139**, 13013–13023.
56 J. T. E. Quinn, J. Zhu, X. Li, J. Wang and Y. Li, *J. Mater. Chem. C*, 2017, **5**, 8654–8681.
57 C. C. Stoumpos, D. H. Cao, D. J. Clark, J. Young, J. M. Rondinelli, J. I. Jang, J. T. Hupp and M. G. Kanatzidis, *Chem. Mater.*, 2016, **28**, 2852–2867.
58 F. Hinkel, T. Marszalek, W. Zajaczkowski, S. R. Puniredd, M. Baumgarten, W. Pisula and K. Müllen, *Chem. Mater.*, 2014, **26**, 4844–4848.
59 M. Li, C. An, W. Pisula and K. Müllen, *Acc. Chem. Res.*, 2018, **51**, 1196–1205.
60 F. G. Guijarro, P. Malhotra, G. Gupta, R. Caballero, P. de la Cruz, R. Singhal, G. D. Sharma and F. Langa, *J. Mater. Chem. C*, 2020, **8**, 4763–4770.
61 R. Zheng, Q. Guo, D. Hao, C. E. Zhang, W. Xue, H. Huang, C. Li, W. Ma and Z. Bo, *J. Mater. Chem. C*, 2019, **7**, 15141–15147.
62 J. Lee, J. L. Hernandez, I. Pelse, J. R. Reynolds and C. Yang, *J. Mater. Chem. C*, 2018, **6**, 10532–10537.
63 R. Mondal, H. A. Becerril, E. Verploegen, D. Kim, J. E. Norton, S. Ko, N. Miyaki, S. Lee, M. F. Toney, J.-L. Brédas, M. D. McGehee and Z. Bao, *J. Mater. Chem.*, 2010, **20**, 5823–5834.
64 J. Luo, X. Wang, L. Fan, G. Li, Q. Qi, K.-W. Huang, T. L. Dexter Tam, J. Zhang, Q. Wang and J. Wu, *J. Mater. Chem. C*, 2016, **4**, 3709–3714.

65 Y.-D. Lin, K.-M. Lee, S. H. Chang, T.-Y. Tsai, H.-C. Chung, C.-C. Chou, H.-Y. Chen, T. J. Chow and S.-S. Sun, *ACS Appl. Energy Mater.*, 2021, **4**, 4719–4728.
66 S. J. Cho, M. J. Kim, Z. Wu, J. H. Son, S. Y. Jeong, S. Lee, J. H. Cho and H. Y. Woo, *ACS Appl. Mater. Interfaces*, 2020, **12**, 41842–41851.
67 S.-H. Lee, B. Lim, M. Pei, H. Yang and Y.-Y. Noh, *J. Mater. Chem. C*, 2018, **6**, 7604–7611.
68 J. Lee, J. Kim, T. L. Nguyen, M. Kim, J. Park, Y. Lee, S. Hwang, Y.-W. Kwon, J. Kwak and H. Y. Woo, *Macromolecules*, 2018, **51**, 3360–3368.
69 A. Tripathi, Y. Ko, M. Kim, Y. Lee, S. Lee, J. Park, Y.-W. Kwon, J. Kwak and H. Y. Woo, *Macromolecules*, 2020, **53**, 7063–7072.
70 C. Du, C. Li, W. Li, X. Chen, Z. Bo, C. Veit, Z. Ma, U. Wuerfel, H. Zhu, W. Hu and F. Zhang, *Macromolecules*, 2011, **44**, 7617–7624.
71 M. Heeney, C. Bailey, M. Giles, M. Shkunov, D. Sparrowe, S. Tierney, W. Zhang and I. McCulloch, *Macromolecules*, 2004, **37**, 5250–5256.
72 H. Usta, C. Risko, Z. Wang, H. Huang, M. K. Deliomeroglu, A. Zhukhovitskiy, A. Facchetti and T. J. Marks, *J. Am. Chem. Soc.*, 2009, **131**, 5586–5608.
73 H. Usta, A. Facchetti and T. J. Marks, *J. Am. Chem. Soc.*, 2008, **130**, 8580–8581.
74 J. Liu, R. Zhang, I. Osaka, S. Mishra, A. E. Javier, D.-M. Smilgies, T. Kowalewski and R. D. McCullough, *Adv. Funct. Mater.*, 2009, **19**, 3427–3434.
75 S. Handa, E. Miyazaki, K. Takimiya and Y. Kunugi, *J. Am. Chem. Soc.*, 2007, **129**, 11684–11685.
76 J. Li, X. Qiao, Y. Xiong, W. Hong, X. Gao and H. Li, *J. Mater. Chem. C*, 2013, **1**, 5128–5132.
77 K. Menekse, P. Chen, B. Mahlmeister, O. Anhalt, A. Kudzus, M. Stolte and F. Würthner, *J. Mater. Chem. C*, 2020, **8**, 15303–15311.
78 Y. A. Getmanenko, T. A. Purcell, D. K. Hwang, B. Kippelen and S. R. Marder, *J. Org. Chem.*, 2012, **77**, 10931–10937.
79 J. Youn, S. Kewalramani, J. D. Emery, Y. Shi, S. Zhang, H.-C. Chang, Y.-J. Liang, C.-M. Yeh, C.-Y. Feng, H. Huang, C. Stern, L.-H. Chen, J.-C. Ho, M.-C. Chen, M. J. Bedzyk, A. Facchetti and T. J. Marks, *Adv. Funct. Mater.*, 2013, **23**, 3850–3865.
80 J. Youn, S. Vegiraju, J. D. Emery, B. J. Leever, S. Kewalramani, S. J. Lou, S. Zhang, K. Prabakaran, Y. Ezhumalai, C. Kim, P.-Y. Huang, C. Stern, W.-C. Chang, M. J. Bedzyk, L. X. Chen, M.-C. Chen, A. Facchetti and T. J. Marks, *Adv. Electron. Mater.*, 2015, **1**, 1500098.
81 B. Sharma, Y. Sarothia, R. Singh, Z. Kan, P. E. Keivanidis and J. Jacob, *Polym. Int.*, 2016, **65**, 57–65.